State Correlations in the Unimolecular Dissociation of Ketene†

Matthew L. Costen,‡,§ Hideki Katayanagi,|| and Gregory E. Hall*,‡

Chemistry Department, Brookhaven National Laboratory, Upton, New York 11973-5000, and Institute for Molecular Science, Myodaiji, Okazaki 444-8585, Japan

Received: April 13, 2000; In Final Form: June 15, 2000

Doppler-broadened absorption spectra of selected rotational levels of singlet CH_2 fragments from the 308-nm photolysis of ketene have been observed by frequency-modulated transient absorption spectroscopy in a slit jet expansion. Nascent Doppler profiles of CH_2 transitions have been analyzed to yield the internal energy distributions of coincident CO fragments at a total energy 2333 cm^{-1} above the singlet dissociation threshold. The vibrational branching ratio of CO ($v = 1$):($v = 0$) is determined in coincidence with selected rotational levels of CH_2. The coincident rotational distributions of CO ($v = 0$) are also estimated and found to differ from simple statistical predictions, revealing a relative deficiency of those pairs in which both fragments have a low internal energy.

1. Introduction

The singlet dissociation channel of ketene has become a prototype for the study of barrierless unimolecular decomposition.[1,2] Continuous absorption in the near-ultraviolet, followed by rapid nonradiative conversion from the excited singlet to the ground state, makes it possible to prepare isolated molecules with a laser-selected energy at a well-defined time. This fortunate photophysics has permitted energy-dependent decomposition rates and product distributions to be measured for this particular reaction more conveniently than for most ground-state reactions. The extensive experimental investigations have encouraged similarly extensive theoretical work on this particular reaction, now one of the most completely characterized unimolecular reactions known. New experiments interrogating the correlated product state distribution, including the present work, build on this foundation, addressing old questions in new ways.

Following dipole-forbidden optical excitation from the $^1A_1$ ground state (S_0) to the $^1A_2$ excited state (S_1), ketene undergoes a radiationless transition to S_0, followed either by dissociation to CH_2 ($\tilde{a}\ ^1A_1$) + CO ($X\ ^1\Sigma^+$) or by intersystem crossing to the triplet and dissociation over a barrier to CH_2 ($X\ ^3B_1$) + CO ($X\ ^1\Sigma^+$). Recent ab initio calculations confirm this general picture of the nonadiabatic interactions and state couplings.[3] Rate constants for the singlet channel have been measured over a wide range of excess energies from threshold to 2500 cm^{-1} via both photofragment excitation (PHOFEX) spectroscopy near threshold[4,5] and picosecond spectroscopy of CH_2 at higher energies.[6] The rates near threshold are very well described by phase space theory (PST).[7,8] At higher energies, the dissociation rate increases less rapidly than the PST prediction. The observed rates can be accounted for with a tightening transition state using variational RRKM theory.[9−11] At an energy 2500 cm^{-1} above the singlet threshold, PST overestimates the dissociation rate by about a factor of 10. Product state distributions of both CO[12−14] and CH_2[15,16] have been measured using laser-induced fluorescence (LIF) as a function of excess energy. Early measurements of CO product rotational distributions[12,13] were in good agreement with PST at energies up to 2500 cm^{-1}, although the superposition of coincident singlet and triplet CH_2 channels led to some uncertainty in the interpretation. Subsequent measurements of CO ($v = 1$), where the triplet CH_2 contribution is negligible, showed subtle deviations from the PST rotational distributions, increasing at higher energy.[14] The singlet CH_2 state rotational distributions follow PST near threshold, but become much colder than the PST predictions at higher excess energies.[15,16] The yields of vibrationally excited fragments, both CO ($v = 1$)[17] and the first bending excitation of CH_2 (v_1,v_2,v_3) = (0,1,0) are found to exceed PST predictions, an effect attributed to vibrational adiabaticity in the conserved modes and predicted by the separate statistical ensembles (SSE) model,[18] as well as variational RRKM, if the populations of the conserved modes at the transition state are assumed to be the same as those in the final products.[9]

The global product distributions can be considered orthogonal projections of a two-dimensional coincident state distribution, as illustrated in Figure 1. The triangular region in the upper right square shows the correlated energy states of the singlet channel, with the diagonal boundary representing the available energy limit at 308 nm. Each black symbol represents a rotational state of CO ($v = 0$) with a coincident rotational level of CH_2 (0,0,0). An overlapping green set of symbols represents the possible states of the (0,1,0) bending excitation of CH_2 with its possible coincident CO states. A red cluster of symbols in the lower right of the triangle shows the possible pairs of states including CO ($v = 1$). At this energy, 35 rotational states of CO ($v = 0$) and 10 rotational states of CO ($v = 1$) combine with about 80 CH_2 (0,1,0) states and about 220 CH_2 (0,0,0) states to produce almost 6000 accessible coincident pair channels, each depicted by a symbol on this plot. This plot could be expanded to include the triplet CH_2 channel by adding the term value of singlet CH_2 ($\tilde{a}$) to the CH_2 internal energy scale shown on the vertical axis and moving the origin down to the

† Part of the special issue "C. Bradley Moore Festschrift".

* Author to whom correspondence should be addressed. E-mail: greghall@bnl.gov. Telephone: (631) 344-4376. Fax: (631) 344−5815.

‡ Brookhaven National Laboratory.

§ Present address: Department of Chemistry, Heriot-Watt University, Edinburgh, EH14 4AS, U.K.

|| Institute for Molecular Science.

10.1021/jp001389f CCC: $19.00
Published on Web 07/21/2000

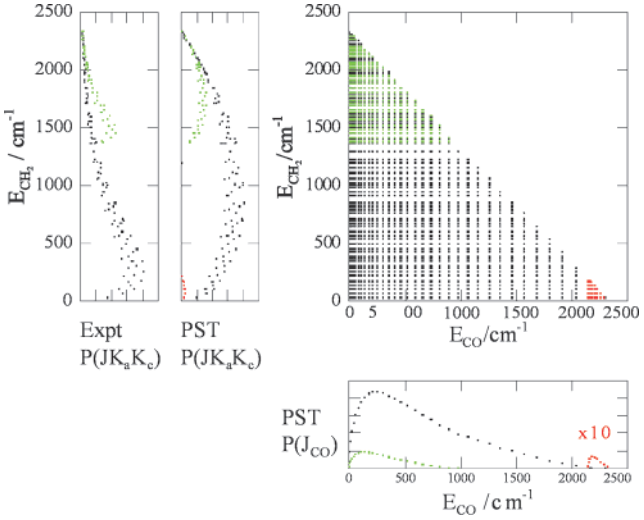

Figure 1. Correlated final states of ketene dissociation. Three vibrational channels are color-coded. Black, CO ($v = 0$) + CH_2 (0,0,0); green, CO ($v = 0$) + CH_2 (0,1,0); and red, CO ($v = 1$) + CH_2 (0,0,0). Global state distributions are projections of probability from the triangle onto the CO and CH_2 energy axes. Black and green measurements on CH_2 can be made of (0,0,0) and (0,1,0) total populations; low-energy CH_2 states can have a partial contribution from the red channel. Black and red measurements of CO can be made of ($v = 0$) and ($v = 1$) total populations; low-energy CO states have a partial contribution from the green channel. PST state distributions are illustrated for CO and CH_2. The experimental CH_2 distributions more closely resemble Boltzmann distributions than the PST distribution, whereas the CO distribution is not greatly different from PST.

zero point of the triplet CH_2 (X) state. It is evident that any CO state that can be produced in the singlet channel could, in principle, also be produced in coincidence with triplet CH_2.

The distribution of probability within this triangle provides a more revealing test of the fragmentation process than its projections onto the single-particle axes.[19,20] Phase space theory assigns the weight of each energetically accessible coincident channel to be proportional to the number of ways the two fragment angular momenta can couple with an orbital angular momentum, consistent with the total angular momentum of the parent molecule. (For the fragmentation of a low angular momentum parent molecule, the additional energetic constraint due to the centrifugal barrier is practically negligible.) The usual product state distributions are projections of the density of this two-dimensional grid onto the CO energy axis or the CH_2 energy axis, as shown in the plots below and to the side for a PST weighting of coincident states. Green symbols to the left and red symbols below respectively show the rotational populations of CH_2 (0,1,0) and CO ($v = 1$). CO states with internal energies less than about 1000 cm^{-1} may have contributions from two vibrational channels of coincident singlet CH_2. The green points in the CO distribution illustrate the partial contribution made by CO with vibrationally excited CH_2 partners to the total CO ($v = 0$) population, shown in black. Similarly, the red points in the CH_2 distribution indicate the partial contribution of CH_2 with vibrationally excited CO partners to the total CH_2 (0,0,0) population, shown in black. The 3:1 ratio of ortho:para nuclear spin modifications of the CH_2 fragments is suppressed for graphical simplicity in Figure 1, in which only the ortho (nuclear spin = 1) modifications of CH_2 states are plotted. One of the most striking deficiencies of PST for ketene dissociation at increasing energies is the strong deviation of experimental CH_2 state distributions from the PST prediction, whereas the CO distribution remains approximately statistical. The observed CH_2 rotational distributions were found to resemble Boltzmann distributions,[15,16] with an increasing effective temperature at higher available energies, approximately 700 K for CH_2 (0,0,0) at the 2333 cm^{-1} available energy of 308-nm excitation. The far left panel of Figure 1 illustrates the experimentally determined, Boltzmann-like distributions observed.

State-resolved velocity measurements such as Doppler spectroscopy, time-of-flight methods, or ion imaging provide ways of viewing slices rather than projections of the correlated state distributions.[19] Metastable CO time-of-flight methods have been developed and applied to the 308-nm dissociation of ketene by Wodtke and co-workers.[21,22] These experiments provide vertical slices through the correlated state distribution shown in Figure 1 at spectroscopically selected CO states. The present paper reports the results of Doppler spectroscopy on the singlet CH_2 products, which relate to horizontal slices through the same correlated state distribution produced in the 308-nm dissociation of jet-cooled ketene. Although a complete set of correlated data for either fragment is, in principle, sufficient for reconstructing the full matrix of correlated states, the task is not trivial, and the new orthogonal view is advantageous for identifying qualitative agreements and quantitative differences with previous results. The way in which the dissociation distributes probability among the accessible channels, and in particular the shape of the deviations from the most random PST distribution, gives some insight into energy flow in the dissociating molecule beyond the transition state and the statistical nature of the transition state.

2. Experimental Section

Ketene was synthesized by the pyrolysis of acetic anhydride flowing past a hot filament. Unreacted acetic anhydride and water were removed from the flow in a dry-ice-cooled trap, and the ketene was collected in a liquid-nitrogen-cooled trap downstream. A 10% mixture of ketene in helium was expanded through a pulsed slit jet into a stainless steel chamber. The slit was 115 mm long and 50 μm wide, with a seal actuated by three synchronously driven solenoid-type pulsed valves (General Valve). The constuction of the valve was based on the design of Hu et al.,[23] similar to that described later by Liu et al.[24] The chamber was mounted directly on a 400 ft^3/min Roots blower/rotary pump combination. This provided sufficient pumping capacity to reduce the background pressure between valve firings to $\leq$5 mTorr at 10 Hz, ensuring that the expansion was supersonic in the region probed. The gas pulses had a duration of about 400 μs. The total gas consumption was about 500 std cm^3 min^{-1} at a backing pressure of 650 mbar. We estimate rotational and translational temperatures of 15−20 K in the ketene expansion, on the basis of Doppler spectroscopy of CH_2, as described below.

The CH_2CO was photolyzed by unpolarized 308-nm light from a XeCl excimer laser (Lambda Physik Compex102) propagated along the slit axis about 2 cm downstream from the slit. The singlet CH_2 product was probed at wavelengths near 800 nm using frequency-modulated (FM) transient absorption. Many aspects of the apparatus and method have been described previously;[25,26] only brief additional details are provided here. Continuous light from an Ar^+-pumped Ti:sapphire ring laser (Coherent 899-29) with a bandwidth of <1 MHz was electro-optically modulated, producing sidebands at ±200 MHz from the carrier frequency. The modulated probe beam was then copropagated with the photolysis light along the slit expansion. The probe beam was reflected back through the slit jet sample at a small angle, providing a second absorption path through

the same approximate region, and focused onto a photodiode detector. The 200-MHz beat signal arising from the differential absorption or retardation of the sidebands was filtered, amplified, and mixed with the 200-MHz reference signal in an I&Q demodulator. The resulting transient signals were low-pass filtered (70 MHz), averaged in a digital oscilloscope (LeCroy 9310A), and transferred to a computer for storage. Transient waveforms from 30 photolysis shots were averaged at each 100-MHz step of the probe laser frequency. The archived data can be considered either as laser-frequency-indexed series of transient waveforms or as time-indexed series of FM spectra, acquired in-phase (I) and in quadrature (Q). The I&Q signals are different linear combinations of absorption and dispersion line shapes; a knowledge of the absolute reference phase angle is required to isolate the FM absorption and dispersion components. The phase calibration and correction were achieved using translationally thermalized, Gaussian FM lines in the manner previously described.[25] Relaxed CH_2 lines formed from the photolysis of ketene in the expansion region of the supersonic jet gave an upper bound to the translational temperature of the beam of 20 K. The spectroscopy of $^1CH_2$ in the $\tilde{b}\ ^1B_1-\tilde{a}\ ^1A_1$ transition is complex, with significant perturbations leading to unpredictable line strengths, rendering assignment of the very large number of observable lines difficult, particularly those with large values of J or K_a. The data presented here were recorded on a selection of previously assigned transitions,[27,28] covering a range of low-$J_{K_aK_c}$ states in the vibrational ground state of CH_2.

A separate glass cell was used in an experiment to measure the translational anisotropy of CH_2 photofragments from thermal ketene samples, in a manner previously described.[26] The cell contained two parallel, 1 in. by 3 in., flat, high-reflectivity mirrors. The vertically polarized probe beam was reflected in a horizontal plane 20 times between these mirrors on its way to the photodiode receiver. The photolysis beam was polarized using a Brewster stack of 10 fused silica plates, passed through a photoelastic modulator (Hinds Instruments PEM 90), and propagated between the multipass mirrors. The timing of the photolysis laser was synchronized with the stress cycle of the PEM and controlled by the data acquisition computer to enable the acquisition of FM Doppler profiles with the linear photolysis polarization alternately parallel or perpendicular to the propagation direction of the probe beam. A slowly flowing thermal sample of neat ketene at 30 mTorr was used for these measurements.

3. Results

3.1. Selection of Rotational Lines. Transient FM spectra of CH_2 photofragments were acquired for a selection of rotational states, mostly using transitions in the $\tilde{b}\ ^1B_1$ (0,8,0) $\leftarrow \tilde{a}\ ^1A_1$ (0,0,0) band. Table 1 lists the transitions used and the rotational energies of the detected CH_2 states. The highest-energy accessible coincident quantum states of CO ($v = 0$ and $v = 1$) are also tabulated, assuming the ketene parent molecule to have no internal energy and using the average vacuum wavenumber of the XeCl excimer emission doublet, 32 449 cm^{-1}. This gives 2333 cm^{-1} of available energy for singlet CH_2 and CO from the zero point of ketene. Vibrationally excited CO can only be produced in coincidence with singlet CH_2 states with a rotational energy less than 190 cm^{-1}. Only spectra for rotational states of the ground vibrational state of CH_2 were recorded, as we were unfortunately unable to identify usable lines originating from the first excited bending state (0,1,0) of CH_2 in the spectral region of our Ti:sapphire laser.[27,28] The highest-energy rotational state of CH_2 for which we could detect usable nascent Doppler spectra was the 6_{52} state. Only a small number of transitions originating from higher-energy rotational states have been assigned. A very weak signal was detected from the 7_{52} state (with 787 cm^{-1} of rotational energy) at 12 264.03 cm^{-1}. Either the population of this state or the line strength of this transition is substantially weaker than for those of lower-energy states. Linear interpolation of effective CH_2 rotational temperatures reported by García-Moreno et al.[15] gives a temperature of about 700 ± 100 K for 308-nm excitation. With this distribution, 57 ± 6% of the CH_2 (0,0,0) population would have a rotational energy in the energy region included in our sample. This incomplete coverage limits our ability to construct the entire correlated state distribution from our measurements, but not as severely as if the CH_2 product state distributions were well described by the much hotter PST distributions.

TABLE 1: CH_2 Transitions Used in the $\tilde{b}\ ^1B_1$ (0,8,0) ← $\tilde{a}\ ^1A_1$ (0,0,0) Band

transition	frequency (cm^{-1})	energy (cm^{-1})	j_{max} CO $v = 0^b$	j_{max} CO $v = 1^b$	$(v = 1):(v = 0)^c$
$2_{02}-1_{10}$	12 234.82	31.3	34	8	0.23 ± 0.04
$2_{02}-2_{12}$	12 206.550	59.6	33	7	0.16 ± 0.04
$3_{31}-2_{21}$	12 224.50	98.5	33	6	0.18 ± 0.03
$3_{30}-2_{20}$	12 223.25	99.6	33	6	0.17 ± 0.06
2_{02} - 3_{12}	12 134.13	132.0	33	5	0.16 ± 0.03
$3_{31}-3_{21}$	12 164.49[a]	158.5	33	4	0.09 ± 0.04
$4_{31}-3_{21}$	12 230.21[a]	158.5	33	4	0.09 ± 0.04
$4_{04}-4_{14}$	12 204.09	170.4	33	3	0.06 ± 0.02
$5_{05}-5_{15}$	12 204.19	247.9	32	closed	0.0
$4_{04}-5_{14}$	12 070.10	304.4	31	closed	0.0
$6_{06}-6_{16}$	12 206.546	339.7	31	closed	0.0
$5_{42}-6_{52}$	12 294.95	655.2	29	closed	0.0

[a] These transitions are from a different vibrational band, terminating in a state of mixed $\tilde{b}$ (0,11,0) and $\tilde{a}$ (0,9,0) character. [b] Highest rotational level of CO energetically allowed from 308-nm excitation of ketene in its lowest nuclear-spin-conserving state. [c] Experimental ratio of CO vibrational states produced in coincidence with each CH_2 rotational state.

Figure 2 shows representative FM Doppler profiles across the range of states probed. These spectra were selected from the transient data with a time gate 50−100 ns following the photolysis and phase corrected to remove small contributions of dispersion.[25] Multiple scans of each transition were taken and were found to be consistent from day to day. The spectra of the weaker lines shown are averages of several scans to improve the signal-to-noise ratio. Some partially overlapping lines were included in the analysis. As long as the separation of line centers exceeds the maximum Doppler shift by more than twice the modulation frequency, then at least half of each antisymmetric line can be observed without interference from the neighboring line. It is immediately evident that only the lowest rotational states of CH_2 show "spikes" near the line center that are associated with the coincident CO ($v = 1$) channel. Less striking inflections in the direct absorption line shapes were reported earlier[27] and similarly interpreted as a probe of the vibrational branching ratio of CO ($v = 1$):($v = 0$) in coincidence with selected CH_2 states. With the cooling of the parent internal energy in the slit jet and the signal improvements associated with the use of frequency modulation, the present Doppler measurements permit a more careful analysis than was previously possible.

3.2. Controls and Characterization of Doppler Profiles. The shape of a Doppler profile of a photofragment probed by LIF or absorption spectroscopy is the subject of an extensive literature.[29−32] Special considerations for FM Doppler spectros-

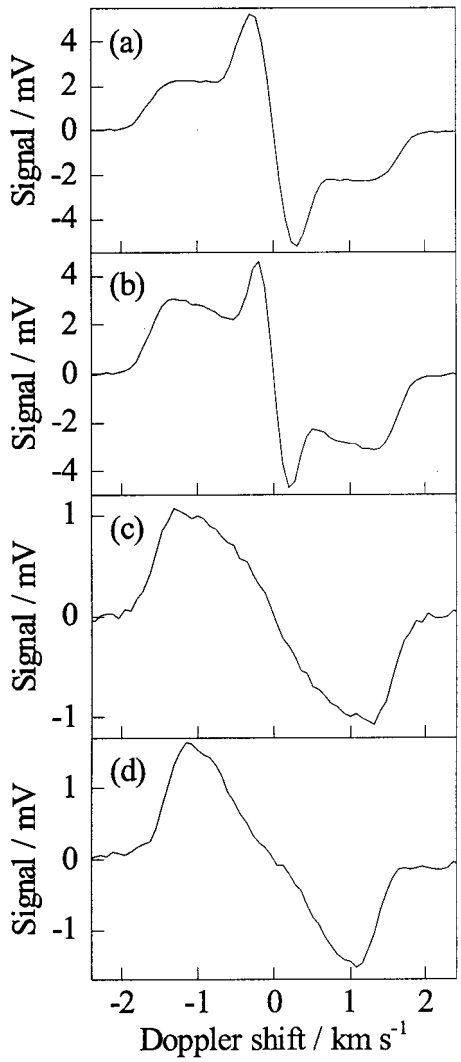

Figure 2. Nascent FM Doppler spectra of selected rotational states of singlet CH_2. The $J_{K_aK_c}$ quantum numbers and rotational energies of the detected CH_2 states are (a) 2_{12}, 60 cm^{-1}; (b) 4_{14} , 170 cm^{-1}; (c) 5_{15}, 248 cm^{-1}; and (d) 6_{52}, 655 cm^{-1}. The detuning of the laser frequency is expressed in this and subsequent figures as an equivalent Doppler shift in velocity units.

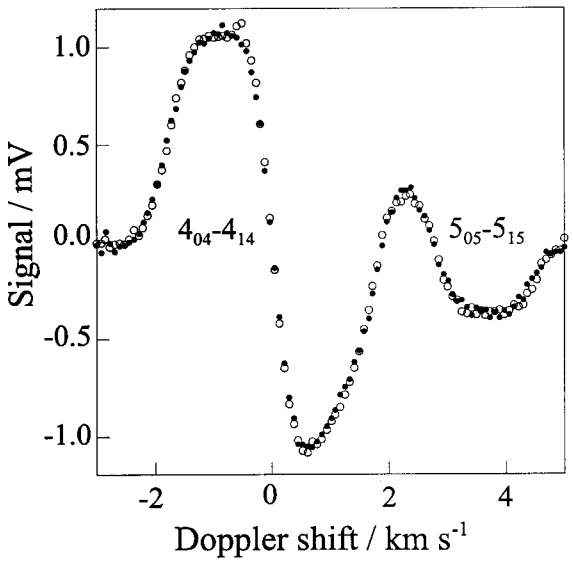

Figure 3. Test for velocity anisotropy of CH_2 fragments from room-temperature dissociation of ketene at 308 nm. Interleaved measurements are shown for two pump−probe geometries, switching the linear polarization direction of the photolysis laser. ●, photolysis laser polarization parallel to probe propagation direction; ○, photolysis laser polarization parallel to probe polarization direction.

copy have been addressed in refs 25 and 26 and in a forthcoming review article.[33] In general, the Doppler profile will depend on the speed distribution of the detected fragment, its angular distribution, and its rotational polarization. The speed distribution is directly related to the internal energy distribution of the undetected cofragment. Each correlated state channel can display a velocity anisotropy due to a correlation between $\boldsymbol{\mu}$, the transition dipole moment of the parent molecule at the time of absorption, and the final fragment velocity, **v**. The rotational polarization is the anisotropy of the fragment angular momentum, **j**, which may be correlated with **v** and/or $\boldsymbol{\mu}$. Several control experiments indicate that both velocity anisotropy and rotational polarization have a negligible effect on the observed Doppler profiles of the detected CH_2 fragments.

3.2.1. Velocity Anisotropy. A sensitive test for velocity anisotropy is to compare Doppler profiles measured with the probe laser propagating parallel and perpendicular to the pump laser polarization vector. The parallel geometry is unfortunately inaccessible in our slit jet with collinear pump and probe laser beams. Accordingly, we have used a low-pressure thermal sample of ketene in a multipass cell and switched the polarization of the photolysis laser using a photoelastic modulator to acquire FM Doppler profiles in these two geometries, as described in a previous study.[26] The blended pair of lines $4_{04}-4_{14}$ and $5_{05}-5_{15}$ is compared in Figure 3 for the two photolysis polarizations. There is no systematic difference with the polarization geometry that can be attributed to a nonvanishing anisotropy. A value of the anisotropy parameter, β, as large as ± 0.1 would result in a clearly visible difference above the noise level shown.

The comparison of signals acquired from photolysis of a thermal sample of ketene should be used with some caution when the dissociation of a jet-cooled sample is considered. Rotation of the excited ketene prior to dissociation can reduce the fragment anisotropy relative to the value that would have been observed in a prompt dissociation.[32,34] The dissociation time scale observed in jet-cooled ketene excited to an energy 2500 cm^{-1} above the singlet threshold was about 100 ps; effusive samples were found to dissociate only about 20% faster.[6] This dissociation is more than 10 times slower than a typical rotational period for ketene at 20 K and about 50 times slower than a typical rotation at room temperature. Additional depolarization mechanisms may be related to the vibronically induced nature of the $^1A_1$ to $^1A_2$ (A″) transition and a distribution of geometry changes following excitation. In any case, the velocity anisotropy is evidently very small, and we proceed in the analysis of the CH_2 Doppler spectra as if the fragmentation were strictly isotropic.

3.2.2. Rotational Polarization. In the limit of isotropic fragment velocities, the only rotational polarization that can be observed is the **v**−**j** correlation, parametrized by the bipolar moment $\beta_0^0(22)$.[29] This correlation has been observed for the CO fragment by Morgan et al.[22] but is not expected to be strong for CH_2, because the magnitude of its angular momentum is smaller than the average angular momentum of its CO cofragment.[35,36] We can confirm that the **v**−**j** correlation of the detected CH_2 states is small by comparing Doppler line shapes for different rotational branch transitions probing the same rotational state. Profiles acquired on the $4_{31}-3_{21}$ and $3_{31}-3_{21}$ transitions are shown in Figure 4, and do not differ by an amount in excess of the experimental noise. Thus, there does not appear

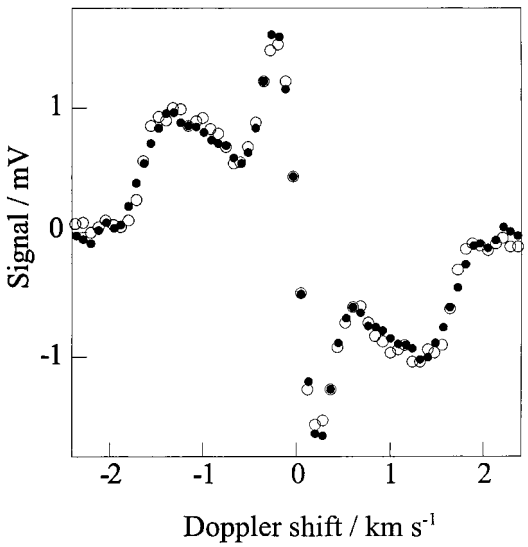

Figure 4. Test for rotational polarization of CH_2 fragments. Comparison of R- and Q-branch transitions $4_{31}-3_{21}$ (●) and $3_{31}-3_{21}$ (○). The signal from the weaker Q-branch transition has been scaled up by a factor of 3.2 to compare the shapes, which are indistinguishable.

to be a measurable **v**−**j** correlation in this CH_2 fragment, typical of the those that we interrogate in this work.

3.2.3. Nuclear Spin Effects. Conservation of nuclear spin in the dissociation produces ortho and para modifications (K_a + K_c = odd and even, respectively) of the CH_2 fragments in the same 3:1 ratio as in the parent ketene molecule.[37] For this reason, most of the states we chose to measure were the more-populated ortho states. One comparison of spectra measured on the $3_{30}-2_{20}$ and $3_{31}-2_{21}$ transitions showed identical Doppler line shapes within the experimental noise, suggesting no significant variation with the nuclear spin modifications between these states differing in energy by about 1 cm^{-1}. Although the 9 cm^{-1} difference in minimum internal energies of the ortho and para parent molecules is not evident in these spectra, we include the energetic consequences of nuclear spin conservation in the thermal averaging described in sections 3.3.1 and 3.3.2 below.

3.2.4. Jet Cooling Conditions. One final additional set of measurements was performed to assess the effective cooling in the slit jet. The photolysis laser beam was displaced toward the nozzle in order to dissociate ketene in the dense collision zone of the slit jet, while translationally cooled CH_2 was probed in a region 2 cm downstream. Reaction and quenching through collisions occur rapidly enough that it was difficult to calibrate relative populations of the different rotational states of singlet CH_2, but the line shapes were relaxed to Gaussian forms with a width characteristic of 15−20 K by the time the fragments reached the probe volume. Other measurements under comparable conditions in this apparatus, using CHBr fragments from the photodissociation of $CHBr_3$, yielded temperatures of 20 ± 5 K for both rotational distributions and translational temperatures.[38] Ketene has several low-frequency vibrational modes that could contribute disproportionately to threshold dissociation channels. We believe that the jet expansion conditions provide good vibrational cooling on the basis of the abrupt disappearance of the spike in the Doppler spectra as the energy of the CH_2 increases above the maximum energy for which CO ($v = 1$) can be formed. A nearby pair of nascent rotational lines probing the 4_{14} and 5_{15} states of CH_2 is illustrated in Figure 5. The 4_{14} state is nominally 20 cm^{-1} below the maximum for coincident CO ($v = 1$), and the 5_{15} state is 58 cm^{-1} above the cutoff, neglecting parent energy. No trace of CO ($v = 1$) is evident in

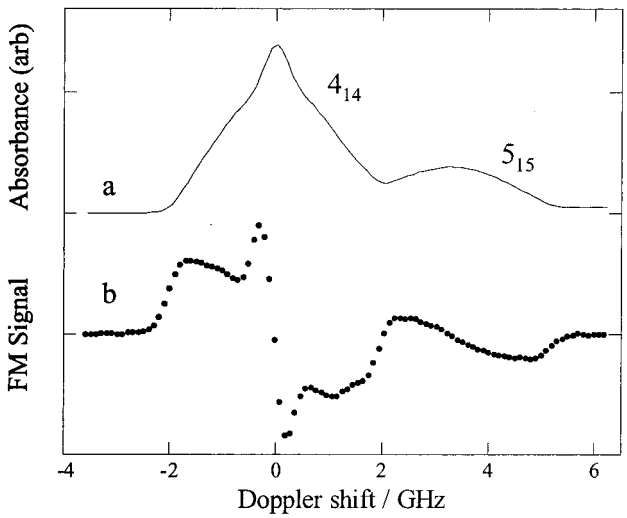

Figure 5. Adjacent rotational lines of CH_2 display a slow component attributed to CO ($v = 1$) produced in coincidence with CH_2 in the 4_{14} but not the 5_{15} rotational state, 78 cm^{-1} higher in energy. (a) FM spectrum transformed to absorption and (b) raw FM spectrum.

the Doppler spectrum of the higher-energy CH_2 state, suggesting that the parent energy selection is good and, in particular, that hot bands are not a significant concern. The shape and width of the sharp feature in the center of the FM spectrum of the 4_{14} state in Figure 5b are primarily determined by the parent speed distribution of ketene in the slit jet. An assumed parent temperature as low as 10 K or as high as 30 K leads to significantly worse fits to this part of the spectrum than that obtained with a best-fit temperature of 20 K. In analyzing the nascent CH_2 Doppler profiles, therefore, we assume a 20-K distribution of parent internal energies and use a convolution of trial center-of-mass speed distributions with a 20-K Gaussian parent velocity to compare to our laboratory-frame Doppler measurements.

3.3. Correlated State Distributions. With the simplifications of negligible velocity anisotropy and rotational polarization, the Doppler profile of a state-selected CH_2 fragment is easily computed from a trial distribution of coincident CO states. Energy conservation in the center-of-mass (COM) frame gives the translational energy in terms of the photon energy, the bond dissociation energy for the singlet channel, and the internal energies of parent and fragments.

$$E_T = h\nu + E_{int}(CH_2CO) - D_0(CH_2 - CO) - E_{int}(CH_2) - E_{int}(CO) \quad (1)$$

For a selected internal energy state of CH_2, each accessible coincident CO state produces a characteristic translational energy, broadened only by the distribution of parent internal energy and the bandwidth of the photolysis laser. The CH_2 fragment's COM velocity distribution, $f(v)$, is thus a sum of narrowly peaked speeds, one for each coincident CO state. Assuming an isotropic velocity distribution, normalized according to

$$1 = 4\pi \int_0^\infty f(v) v^2 \, dv \quad (2)$$

the corresponding Doppler-broadened absorption spectrum is given by[39]

$$D(w) = \int_{|w|}^\infty \frac{f(v) v^2}{2v} \, dv \quad (3)$$

Here, w is the velocity-equivalent Doppler shift, the fractional detuning from the line center times the speed of light. In the laboratory frame, the Doppler profile is broadened by a one-dimensional Gaussian convolution with the parallel component of the parent molecules' thermal velocity distribution, giving a broadened spectrum we denote as $D'(w)$. Finally, for FM detection, one measures a finite difference spectrum. Each point in the FM spectrum is related to the difference in absorption at the optical frequencies of the sidebands, shifted by integer multiples of δ (in velocity units) away from the main laser frequency.

$$\mathrm{FM}(w) \propto D^1(w-\delta) - D^1(w+\delta) + \frac{J_1J_2 + J_2J_3}{J_0J_1 + J_1J_2}[D^1(w-2\delta) - D^1(w+2\delta)] \quad (4)$$

Small corrections are included for higher-order sidebands,[40] the first term of which is shown, where J_n is the nth-order Bessel function of argument M, the modulation index used in the frequency modulation,[33] typically 0.9 in our experiments.

3.3.1. Trial Doppler Fits to PST. To illustrate this procedure, we take the parameter-free PST distribution of CO in coincidence with CH_2 in a quantum state high enough in energy to permit only CO ($v = 0$) and compute the corresponding FM Doppler spectrum. Figure 6 shows the PST state distribution and the resulting FM Doppler spectra for the 5_{14} state of CH_2, compared to experiment. The least-constrained version of PST has an impact parameter limited only by angular momentum conservation, that is, the centrifugal barrier is neglected. The PST CO rotational and vibrational distributions coincident with each particular CH_2 state probed were calculated, including a sum over a Boltzmann-weighted rotational distribution of ketene, using a prolate symmetric top approximation and a rotational temperature of 20 K and including conservation of nuclear spin. The dashed curves in Figure 6a,b show the results of this calculation. Including the centrifugal barrier in the form of a maximum impact parameter, $b_{max} = 4$ Å,[41] results in a reduction of the last few otherwise open channels, as shown with the solid lines of Figure 6a and b. The PST distribution of coincident CO states from a cold ketene parent is characterized by a linear increase with j(CO) until j(CO) = j(CH_2), with a constant probability at higher j(CO) until the energy limit is reached. The centrifugal barrier produces a more gradual falloff in the last few accessible CO states, and the finite temperature of the ketene sample (with its nonzero values of total angular momentum) softens the abrupt change of slope at j(CO) = j(CH_2). The PST simulations of FM Doppler spectra are conspicuously sensitive to the small population of the minimum translational energy channels, but the qualitative discrepancy between experiment and PST is also strong in regions of the spectrum away from the line center. It is worth emphasizing that this mostly flat rotational distribution of PST, not reproduced in our measurements, is also a strict prediction of several generalized statistical models, including SSE,[18] CPST,[14] and an early generalization of variational RRKM for treating product distributions.[9] Identifying the specific deviations from the PST reference case is in the spirit of the adiabatic and nonadiabatic treatment of exit channel effects on capture rates of Nikitin and Troe.[42] We discuss the nature of these deficiencies below, but now describe a method of finding coincident rotational distributions that do agree with the observed spectra.

3.3.2. Rotational State Distributions from Forward Convolution. The failure of PST to predict the observed line shapes leads us to extract the rotational state distributions from the observed spectra. We have explored several approaches to this. For the rotational states of CH_2 with only CO ($v = 0$) in coincidence, we construct a set of basis functions in the space of FM Doppler spectra, one for each energetically allowed rotational state of CO, including the broadening due to parent internal energy and the transformation from COM to lab frame. A linear combination of these functions is sought that best matches the observed spectra. The normal equations are highly singular, as the low rotational states of CO produce very similar contributions. Singular-value decomposition (SVD)[43] with retention of the most significant components of the fit provides a first-order, unbiased estimate of the coincident CO rotational distribution. Figure 7a shows the SVD fit to the same data previously shown in Figure 6. The coincident state distribution produced from the first six terms of the SVD fit is shown with symbols in Figure 7b. The inclusion of four or fewer terms leaves systematic errors in the fit to the spectrum; the inclusion of eight or more terms produces oscillations in the derived state distribution.

An alternative means of deriving the coincident state distribution underlying the measured Doppler spectrum is to adjust a small number of parameters in a flexible, but plausible,

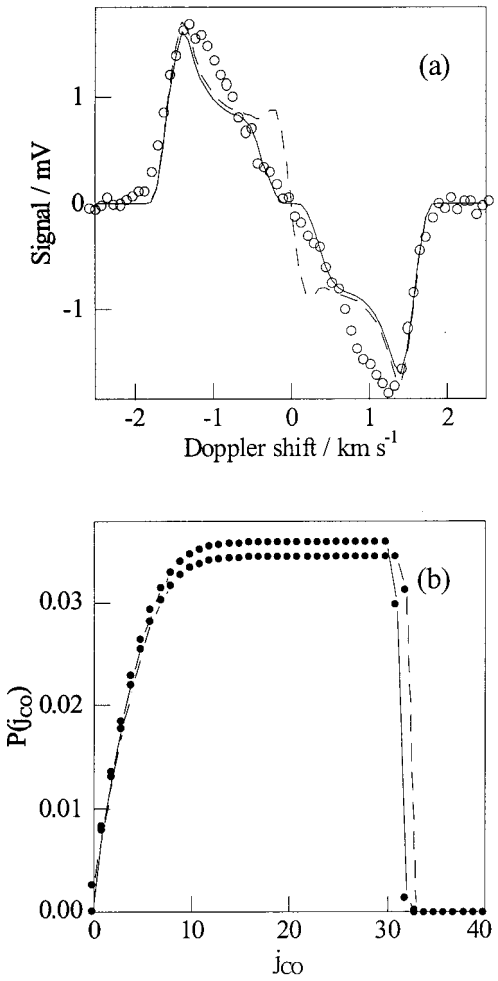

Figure 6. FM Doppler spectra for CH_2 rotational state 5_{14}. (a) Comparison of observed (symbols) and simulations, scaled to a common maximum. Solid line is PST calculation with a 4-Å b_{max}. Dashed line is PST calculation with $b_{max} = \infty$. (b) PST distribution of CO ($v = 0$) rotational states in coincidence with the 5_{14} level of CH_2 from a 20 K sample of ketene excited at 308 nm, leading to the simulations in panel a. The dashed line neglects the centrifugal barrier; the solid line shows the effect of a 4-Å maximum impact parameter.

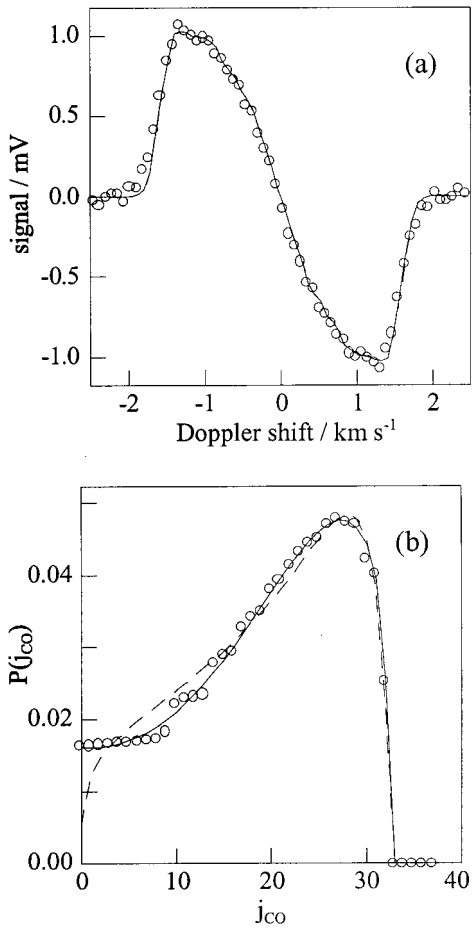

Figure 7. Three least-squares fits to a CH_2 5_{15} FM Doppler profile. (a) Data (symbols) and fits (indistinguishable solid lines). (b) Coincident distribution of j_{CO} derived by three different least-squares methods. Symbols are from a six-term SVD solution to the underdetermined 32 linear equations; the solid line is a fit to a three-parameter function; the dashed line is a fit to a four-parameter function.

functional form for $P(j_{CO})$. We tried several such functions, the first inspired by the functional form of prior distributions in polyatomic dissociations

$$P(j_{CO}) = f_r(j_{CO})^a\,[1 - f_r(j_{CO})]^b \tag{5}$$

where

$$f_r(j_{CO}) = \frac{E_{rot}(j_{CO})}{E_{h\nu} - D_0{}^0(CH_2CO) - E_{CH_2}} \tag{6}$$

and a and b are parameters to be optimized. This functional form is not quite flexible enough to fit the form of the PST distribution, and systematic differences were found in many cases between our best fits and the measurements using this two-parameter function. We found that adding an additional adjustable constant term to all accessible rotational states provided a three-parameter form that could represent the PST distribution, as well as all of our experimental spectra, for the $v = 0$ component of the coincident CO distribution. The result of this three-parameter fit is compared to the SVD fit in Figure 7. The simulated Doppler spectrum is indistinguishable from the SVD fit, and the corresponding state distribution is shown by the solid line in Figure 7b.

A third functional form was implemented, with two adjustable exponential factors combined with the form of eq 5 to give additional flexibility to the shape of the low- and high-energy regions of $P(j_{CO})$. The results of this four-parameter fit are also shown in Figure 7. Not surprisingly, the optimum fit to the spectrum is again indistinguishable. The best coincident state distribution is shown in Figure 7b with the dashed line. The qualitative similarity of the six-term SVD solution and the three-parameter and four-parameter fits gives a feel for the required features and uncertainties of the correlated state distribution that can be derived from the FM Doppler spectrum.

For those CH_2 states with the possibility of being formed in coincidence with CO ($v = 1$), we used the three-parameter representation of the coincident CO ($v = 0$) state distribution and an additional parameter for the ($v = 1$):($v = 0$) branching ratio. The low translational energy of CH_2 formed in coincidence with CO ($v = 1$), along with the close energy spacing of the low-j_{CO} energy levels leads to high sensitivity to the magnitude, but low sensitivity to the shape, of the CO ($v = 1$) contribution to the CH_2 Doppler profiles. Therefore, we have chosen to use the PST shape for the CO ($v = 1$) contribution. The available energy is only 190 cm^{-1} above the $v = 1$ threshold, an energy such that the CO ($v = 1$) rotational distributions should still be well described by a loose, vibrationally adiabatic transition state[13,14] and a distribution of CO states adequately represented by PST.

An example of a two-component fit is shown in Figure 8 for the 4_{14} state of CH_2. The shape of the coincident CO rotational distribution for the $v = 0$ component is very similar to that derived from higher-energy CH_2 states. The amplitude of the $v = 1$ component, shown by the dashed line, reflects a total population of 0.07 relative to the normalized $v = 0$ population. Without including prior information in the fits, the contribution of slow CH_2 with coincident CO ($v = 1$) is not easily distinguished from the the contribution of slow CH_2 formed in coincidence with the last one or two energetically accessible rotational states of CO ($v = 0$). Our chosen analysis method rejects, by construction, what we consider unlikely rotational distributions of CO ($v = 0$), with local maxima in the one or two highest accessible rotational states, even though such distributions could be found that fit the data as well as our preferred analysis.

3.3.3. Vibrational Branching Ratios. The vibrational branching ratios derived from the fitting routine for the various states probed are listed in Table 1. The global CO ($v = 1$):($v = 0$) vibrational branching ratio at this energy has been measured[17] to be 0.022 ± 0.004. This is inconsistent with PST, which predicts a much lower branching ratio of 0.006, but is consistent with the SSE and variational RRKM predictions. Our experimental state-specific branching ratios can be combined to yield a global branching ratio for comparison to the LIF experiments in the following fashion. The CO vibrational branching ratio for unobserved CH_2 states with energies below 200 cm^{-1} was interpolated using the ratios in Table 1, assuming that the $v = 1$ fraction depends only on the energy of the CH_2 state. The global rotational distribution of singlet CH_2 can be empirically described by temperatures for the (0,0,0) and (0,1,0) vibrational levels of 700 K ± 150 K[15] and 315 K ± 100 K,[16] respectively, with a vibrational branching ratio of 1:0.24. The global CO vibrational branching ratio can thus be formed by a sum over the relevant levels using the CH_2 Boltzmann populations and the interpolated coincident state branching ratios. The result is a global CO ($v = 1$):($v = 0$) branching ratio of 0.015 ± 0.005, consistent with that measured by CO LIF.

The state-specific CO branching ratios are remarkably close to the PST values. The SSE model predicts PST-like rotational

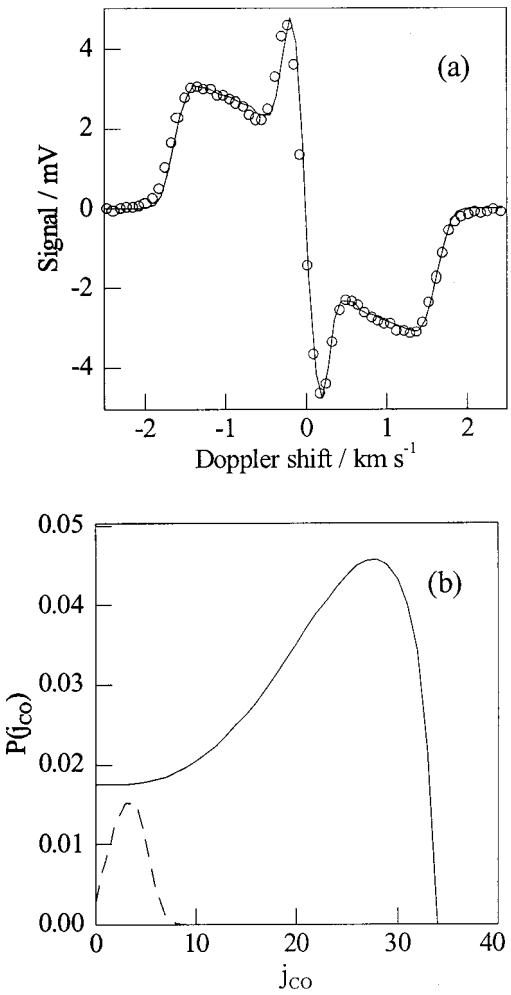

Figure 8. Sample fit to FM Doppler profile for CH_2 4_{14} state. (a) Data (symbols) and fit (line). (b) Coincident rotation distribution for CO ($v = 0$) component, solid line; coincident distribution for CO ($v = 1$) component, dashed line. This fit gives 0.07 for the vibrational branching ratio of CO produced in coincidence with this CH_2 state, the ratio of areas under the dashed and solid curves.

distributions within each vibrational channel, but with a roughly 3-fold difference in vibrational branching ratio. For each coincident state, SSE thus predicts a vibrational branching ratio three times larger than PST, clearly inconsistent with the experimental result. The rotationally resolved vibrational branching ratios should not, however, be considered a naturally useful diagnostic of the unimolecular dynamics. Because each different vibrational product channel can be considered as an independent process, it is more useful to characterize the relative branching among all the vibrational channels, summed over rotation, and the joint rotational distribution within each vibrational channel, as these evidently represent approximately uncoupled steps of the reaction. The fortuitous correctness of the PST state-specific vibrational branching ratios results from an underestimate of the total CO ($v = 1$) population and a conceptually unrelated, but similarly large, underestimate of the fraction of the CH_2 states produced in the CO ($v = 0$) channel with an energy low enough to have CO ($v = 1$) as a possible partner. Similarly, the SSE values of the rotationally resolved vibrational branching ratios are incorrect because of an inappropriate rotational weighting of the correct total vibrational branching ratios. Nevertheless, the observed state-resolved branching ratios serve as primary information in the interpretation of experimental data. For example, in analyzing the rotational distribution of CH_2 (0,0,0) measured by LIF, one could use the branching ratios of Table 1 to decompose the global distribution into components due to the CO ($v = 0$) channel and a smaller component with a colder rotational distribution due to the CO ($v = 1$) channel.

4. Discussion

4.1. Phase Space Theory and Product State Distributions. One practical reason for studying unimolecular reactions at this level of detail is to explore the limits of confidence for approximate theories of reaction rates. Predictive calculations for the rates of barrierless unimolecular reactions are an important requisite for combustion modeling, for example. Product distributions are, however, only indirectly related to rate theories.[44] The evolution of a molecule from the transition state to separated fragments is an additional dynamical step under the influence of the interfragment potential at different ranges, depending on the energy and the specific choice of transition state. Only in the PST limit, where the transition state is defined at the centrifugal barrier and the anisotropy of the long-range interfragment potential is ignored, does the statistical distribution at the transition state correspond directly to the final state distribution. For other types of transition states, additional assumptions are required concerning conserved, mixed, or dynamically controlled degrees of freedom beyond the transition state.[44,45] The issues of adiabaticity and the fate of transitional modes in the exit channel are central questions of current investigation.[20,46−48]

Phase space theory can occasionally provide a good description of product state distributions, while overestimating the rates. This can happen if the intrafragment interaction is strong enough to randomize the state distribution after passage through an inner transition state. Such effects are clearly seen in NO_2, for example,[48,49] illustrating that the inference of a loose transition state on the basis of only a statistical product state distribution is risky.

For ketene, the situation is reversed: PST is known to provide a poor quantitative description of both rates and product distributions at the energies of the present experiments. The questions to ask, then are how much are the final state distributions influenced by exit channel interactions and how much do they reflect properties of the transition states? Correlated state distributions are useful experimental data in addressing these kinds of questions.[19,20]

Referring back to the triangular plot of correlated states in Figure 1, the distortion from PST of the correlated rotational distribution of the CO ($v = 0$) + CH_2 (0,0,0) channel can be characterized as a shifting of probability down and to the right. The similarity of the observed total CO ($v = 0$) rotational distribution to PST is evidently due to a coincidental compensation of the underestimate by PST of the contribution to the low rotational levels of CO produced along with CH_2 (0,1,0), and an overestimate of the low-j(CO) portion of the vibrationless channel. This same change in shape at higher available energies—a tendency for the rotational distributions to approach a Gaussian form, with reduced population at low rotational levels—has been observed in the global CO ($v = 1$) populations at energies more than 1000 cm^{-1} above the CO ($v = 1$) threshold.[14]

4.2. Constrained Phase Space Theory. The singlet CH_2 state distributions deviate increasingly from PST at higher excess energies, whereas the deviations of the CO rotational state distributions from PST remain minor. These observations led to the reasonable conjecture that the more widely spaced CH_2 rotational levels may uncouple from the transitional modes

sooner along the dissociation path than the CO levels, which remain strongly coupled with the transitional modes. An empirically constrained PST (CPST) was thus proposed,[14] in which the experimental state distribution of CH_2 is used as a weighting function. The CO rotational distribution formed in coincidence with each CH_2 state is computed with PST, but the weight of each CH_2 state is constrained to match the measured CH_2 distribution. This CPST model was found to describe the initial deviations from PST of the total CO ($v = 1$) rotational distribution at energies between 350 and 1000 cm^{-1} above the threshold for forming CO ($v = 1$). At still higher energies, adjustable models provided somewhat better fits.

The measurement of CH_2 Doppler profiles provides a direct test of the assumptions of CPST. A single CH_2 state is spectroscopically selected, and the constraints on the CH_2 population can only affect the scaling and not the shape of coincident CO rotational distribution, which is assumed to follow PST. We observe large, qualitative differences between our Doppler spectra and the PST coincident state distributions. At the 2333 cm^{-1} available energy of our experiments, we note that the CO ($v = 0$) + CH_2 (0,0,0) channel is clearly not described by a single constraint on the CH_2 distribution, just as Wade et al.[14] rejected CPST for the CO ($v = 1$) channel at energies more than 1000 cm^{-1} above threshold. We hope to be able to extend the present measurements to some transitions at longer wavelengths probing the (0,1,0) bending state of CH_2, to test CPST at lower energies, where it has been found to provide better agreement with global CO populations.

4.3. Separate Statistical Ensembles. The SSE model[18] provides a simple prediction of vibrational branching ratios, equivalent to the vibrational prior,[50] combined with a PST prediction of the correlated rotational distribution for each separate vibrational channel. The difference between SSE and PST consists of a rescaling of the relative populations of each coincident vibrational channel without modification of the shape of its correlated rotational distribution. Both rotational and vibrational parts of the model work well for NCNO dissociation.[18] Applied to ketene dissociation, the vibrational branching ratios are well described over a wide range of energy.[13,16] The asymmetrical rotational partitioning between CO and CH_2 at energies more than a few hundred wavenumbers above threshold requires explanation beyond PST and SSE. The improved treatment of vibrations in SSE does not address the rotational problem in ketene dissociation.

4.4. Restricted Phase Space Theory. Most closely related to our current experiments are the state-resolved CO time-of-flight (TOF) measurements of Morgan et al.[22] These experiments probe the distribution of CH_2 internal energies coincident with specific CO states, that is, vertical sections through the triangular plot of Figure 1, compared with our CH_2 Doppler measurements, which give horizontal sections. The TOF data for selected CO states were first reduced by forward convolution methods to a COM translational energy distribution and an energy-dependent value of the $\mathbf{v}-\mathbf{j}$ correlation. PST calculations of the translational energy distributions were found deficient, and additional restrictions to PST were proposed to account for their observations. Restricted PST (RPST) calculates the PST distribution of singlet CH_2 states coincident with a specific CO state subject to the additional constraints of a maximum and a minimum impact parameter, b_{max} and b_{min}, respectively, intended to represent structural information about the transition states leading to specific product channels. These two parameters permit the selective rejection of higher and lower angular momentum states of CH_2. To represent the data, different b_{min} and b_{max} values were selected for each j_{CO}, and for those CO states with coincident CH_2 (0,1,0), a second pair of parameters was used to describe this channel. The parameters selected to match the TOF data were, furthermore, found to produce reasonable agreement with global state distributions.

The angular momentum conservation in PST already explicitly imposes upper and lower bounds on the impact parameters, generally much more restrictive than the upper bound related to a centrifugal barrier. It is instructive to compare the b_{min} and b_{max} parameters used in RPST to describe the correlated state distribution with the bounds implied by angular momentum conservation alone. For graphical simplicity, we replace the diatom plus asymmetric top (CO + CH_2) with a model system of diatom plus spherical top. This simplification provides a unique and monotonic relation between the top energy and angular momentum, avoiding the actual, but immaterial, irregularities of level spacing and *K*-dependent energies. We choose the diatomic rotational constant to be that of CO and the spherical top rotational constant to be 12 cm^{-1}, preserving the coarse-grained density of rotational levels for CH_2. With this model, we use PST to compute the distribution of *l*, the orbital angular momentum, for each coincident rotational channel of a single vibrational channel. The available energy is set to 2000 cm^{-1}, and the total angular momentum is set to 3 to represent a typical value in a cold ketene sample. The results can be plotted as the PST probability of orbital angular momentum for a selected CO state as a function of $j(CH_2)$. Figure 9 shows contour plots of these orbital angular momentum distributions for $j(CO) = 5$, 15, and 25. The projection of this *l* distribution onto the $j(CH_2)$ axis gives the PST coincident state distribution for the selected CO state. The increasing probability of higher *j* states of CH_2 is due to the wider range of allowed orbital angular momenta, as well as the $2j + 1$degeneracy that corresponds to the increasing number of K_aK_c states for each *j* in the spherical top limit.

Fixed values of the impact parameter are represented by curves of l_{max} as a function of $j(CH_2)$ in these plots, proportional to the increasing relative velocity for lower-energy states of CH_2. A value of 4 Å for b_{max} produces the blue upper bounds on *l* shown in Figure 9. This value represents a typical centrifugal barrier,[41] and it can be seen to reject only a small fraction of the phase space at the highest few accessible channels. The much smaller values of b_{max} and b_{min} used to characterize CH_2 (0,0,0) by RPST are represented as red curved upper and lower bounds, respectively, on *l* in the same plots. Only those *l* states in the slice between the red upper and lower bounds are included in the RPST, giving strong leverage over the shape of the permitted CH_2 distributions. The main features of this figure apply to "real" CH_2 as well as its spherical analogue, although the upper and lower bounds on *l* cannot be drawn as a single, sharp line when $j(CH_2)$ does not uniquely determine the energy.

We can compare the coincident CO distributions derived from the our Doppler experiments with the RPST parametrization based on the metastable CO TOF experiments. To do so requires an interpolation of the b_{min} and b_{max} parameters for all CO ($v = 0$) states, followed by a RPST calculation of the full correlated rotational distribution for the CO ($v = 0$) + CH_2 (0,0,0) channel. When transformed to the FM Doppler spectrum for selected CH_2 (0,0,0) states, many of these simulations appear to agree with our experiments even less well than does pure PST. There can be several reasons for this disagreement. The TOF and Doppler experiments are subject to very different transformations from raw data to state distributions, and different features of the state distributions are more tightly constrained in the two

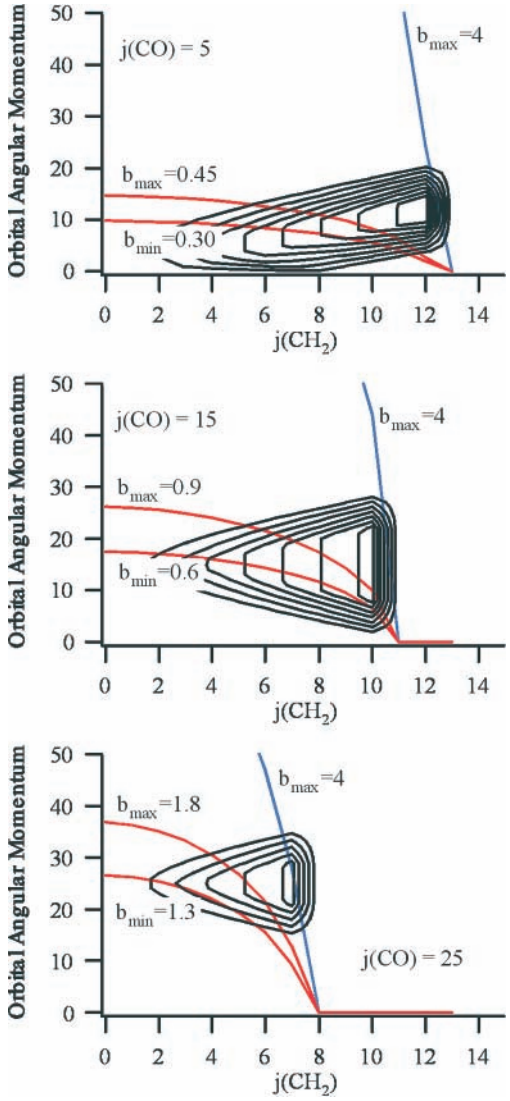

Figure 9. Orbital angular momentum distributions for coincident channels in a diatom plus spherical top model of PST and RPST. Upper and lower bounds on the impact parameter (in Å) correspond to the indicated bounds on *l*.

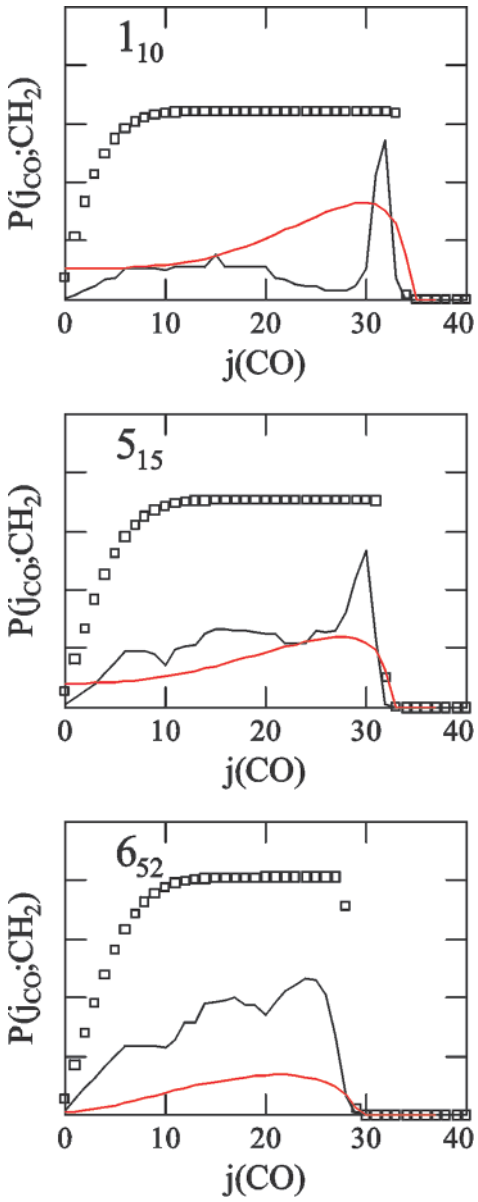

Figure 10. Comparison of CO rotational distributions coincident with selected CH_2 (0,0,0) rotational states: $J_{K_aK_c} = 1_{10}$, 5_{15}, and 6_{52}. The open squares are correlated distributions computed with PST. The solid black lines are computed with RPST using interpolated b_{min} and b_{max} parameters from ref 22. The red lines are the experimental distributions derived from the Doppler profiles. Their shapes have been determined from analysis of the Doppler spectra; normalization relative to PST has been estimated from experimental rates and global product distributions.

experiments. Irregularities introduced in the interpolation of the *j*(CO) dependence of the very sensitive RPST parameters influence the Doppler simulations and not the TOF fits. Some features of the TOF data are not well represented by the RPST parametrization, particularly the time offset in the initial arrival time for the low internal energy CO states, as if the lowest internal energy coincident CH_2 states were missing. Finally, some additional speed-dependent sensitivity corrections due to Doppler selection in the metastable tagging experiments were not included in the original analysis.[51]

Figure 10 compares a selection of CO rotational distributions in coincidence with selected CH_2 (0,0,0) states for PST with a 4-Å centrifugal barrier, RPST using parameters interpolated from the values of Morgan et al.[22] and the empirical distributions derived from our Doppler measurements. Compared to the normalization of PST, RPST shows a state-dependent reduction in probability produced by the additional restrictions on the impact parameter. The total state count of RPST is reduced to about 27% of the PST value, with some coincident channels reduced more than others, as was schematically shown in Figure 9. The lowest-energy CH_2 states are sharply restricted in RPST for all but the highest rotational states of CO, giving a sharp spike at high *j*(CO) for the 1_{10} state of CH_2. Such a distribution would have an unmistakable Doppler signature, which is not observed. Only the shapes and not the absolute magnitudes of the correlated state distributions derived from the Doppler spectra are determined from our measurements. To plot the experimental Doppler curves in Figure 10 on the same scale as the PST and RPST results requires a normalization procedure that uses the experimental rate[6] and global product distributions[15,16] relative to PST. The area under the "observed" correlated state distributions will be smaller than the area under the reference PST distribution by a factor of 8, accounting for the observed reduction in the experimental dissociation rate compared to PST at this excess energy,[17] times a state-dependent correction factor to account for the fraction of the actual CH_2 population formed in each specific state compared to the PST

value. Combined errors in interpolated rates and product distributions used in this normalization may lead to scaling errors as large as 50% for the red curves in Figure 10 relative to the fixed normalization of PST. The *shapes* of the red curves are more accurately determined from the independent Doppler analysis.

In comparisons of our experiments with RPST, an asymmetry of the formulation is evident. One might just as well consider adjusting upper and lower bounds on the impact parameter for each CH_2 state, rather than for each CO state, thereby providing an equally flexible parametrization. It remains unclear to us whether restrictions on impact parameters provide a useful description of the dynamics of energy flow in the exit channel of a barrierless reaction.

4.5. Directly Dissociative Reverse Reactions. The deviations from PST of the correlated rotational state distribution of the vibrational channel with an available energy of 2333 cm^{-1} can be summarized as an overall deficiency of high-energy CH_2 states and a deficiency of those channels with low energy in both CH_2 and CO fragments. The global state distributions from the Moore group, the CO TOF measurements from the Wodtke group, and our CH_2 Doppler profiles are all consistent with these qualitative features. Possible interpretations of the colder CH_2 distributions have been discussed before,[14,15,47] but the suppression of the correlated low-energy pairs is a new observation in the correlated state measurements. These low internal energy correlated rotational states are exactly the ones that are described best by PST at lower energies, when they are the only open channels, yet they fail to contribute according to their statistical weights at higher total energy.

Product interactions in the exit channel, beyond a tightened transition state, can be invoked to describe these effects. A tendency to follow rotationally adiabatic paths would, however, result in a relative excess of the low internal energy channels, contrary to our observations. Some specific dynamic effects of the anisotropic long-range potential may be responsible for the asymmetry of the rotational partitioning, although we are unaware of simple arguments consistent with the observations. Exit-channel dynamical calculations, in the spirit of those proposed by Hamilton and Brumer,[45] would probably be instructive. In this approach, the time-reversed association reaction is considered using classical trajectories. Initial conditions are sampled uniformly in the phase space of the asymptotic fragments at fixed E and J, and approach trajectories are computed under the influence of the interfragment potential. PST rates and product distributions would be exact if all trajectories that were not reflected by the centrifugal barrier reached the deep well of the complex and stuck long enough to randomize the reaction coordinate energy into other modes. Two classes of failed association trajectories can be identified. The first class of trajectories can be characterized by direct repulsion from orientational barriers at larger fragment separation, for example, a turning point in the C−C distance occurring at a C−O−C configuration. The fraction of such medium-range repulsive encounters on a potential with a barrierless minimum-energy path will be closely related to the energy-dependent deviation from PST rates and product distributions, if this is the dominant type of failed association.[42,45,46] To account for the correlated state distributions in this way, one would need to find that high rotational states of CH_2 selectively rebound from CO and that high rotational states of CO selectively associate with low rotational states of CH_2. Theoretical work is required to test this idea.

A second class of failed association trajectories samples the deep well but redissociates after a single vibrational period of the reaction coordinate. This outcome reflects a deviation from the statistical requirement that energy randomization be rapid compared to the reaction. If this direct redissociation is ever significant, it should first be detected for those fragment pairs with a maximum in relative velocity. These are indeed the fragment states that appear to be under-represented in the correlated state distribution at 2333 cm^{-1}. Those fragments that reach an inner turning point and immediately dissociate originate from a part of product phase space that will not be formed in the time-forward dissociation reaction, even though it is permitted by angular momentum and energy conservation. This effect is a failure of the statistical equilibrium assumption and has nothing to do with energy-dependent transition states. It remains an open question as to whether a significant number of such directly dissociative reverse reactions occur between CH_2 and CO at energies as low as 2000 cm^{-1}. Trajectory calculations to test such ideas are in progress.[52] The success of a purely statistical variational RRKM calculation[11] to produce quantitative agreement with experimental rates from threshold up to 6000 cm^{-1} gives some assurance that nonstatistical effects can be neglected. The distinctive correlated state distributions would then need to be explained in terms of specific exit channel interactions.

5. Summary

High-resolution absorption spectroscopy of singlet CH_2 produced in the 308-nm photodissociation of jet-cooled ketene has provided a view of the state distribution of CO produced in coincidence with selected CH_2 states. The results can be compared to "orthogonal" measurements of state-resolved TOF on the CO fragments.[22] There is a qualitative agreement that, for the product channel producing both CO and CH_2 in their vibrational ground states, the correlated rotational channels with low internal energy in each fragment are suppressed relative to PST predictions, as are the high-energy CH_2 states. The results provide a distinctive test for statistical and dynamically corrected statistical theories of unimolecular reaction.

Acknowledgment. Inspiration for this work comes from Prof. C. B. Moore and his colleagues, who have done so much over many years to make ketene synonymous with microcanonical unimolecular dynamics. We are grateful to William Green, Jr., Stephen Klippenstein, Alec Wodkte, and Christopher Morgan for insightful discussions. This work was performed at Brookhaven National Laboratory under Contract DE-AC02-98CH10886 with the U.S. Department of Energy and supported by its Division of Chemical Sciences, Office of Basic Energy Sciences.

References and Notes

(1) Green, W. H.; Moore, C. B.; Polik, W. F. *Annu. Rev. Phys. Chem.* **1992**, *43*, 591.
(2) Moore, C. B. *Faraday Disc*. **1995**, *102*, 1.
(3) Cui, Q.; Morokuma, K. *J. Chem. Phys.* **1997**, *107*, 4951.
(4) Chen, I.-C.; Green, W. H.; Moore, C. B. *J. Chem. Phys.* **1988**, *89*, 314.
(5) Green, W. H.; Mahoney, A. J.; Zheng, Q.-K.; Moore, C. B. *J. Chem. Phys.* **1991**, *94*, 1961.
(6) Potter, E. D.; Gruebele, M.; Khundkar, L. R.; Zewail, A. H. *Chem. Phys. Lett.* **1989**, *164*, 463.
(7) Pechukas, P.; Light, J. C. *J. Chem. Phys*. **1965**, *42*, 3281.
(8) Klots, C. E. *J. Chem. Phys*. **1971**, *75*, 1526.
(9) Klippenstein, S. J.; Marcus, R. A. *J. Chem. Phys.* **1989**, *91*, 2280.
(10) Klippenstein, S. J.; Marcus, R. A. *J. Chem. Phys.* **1990**, *93*, 2418.

(11) Klippenstein, S. J.; East, A. L. L.; Allen, W. D. *J. Chem. Phys*. **1996**, *105*, 118.
(12) Nesbitt, D. J.; Petek H.; Foltz, M. F.; Filseth, S. V.; Bamford, D. J.; Moore, C. B. *J. Chem. Phys.* **1985**, *83*, 223.
(13) Kim, S. K.; Choi, Y. S.; Pibel, C. D.; Zheng, Q.-Z.; Moore, C. B. *J. Chem. Phys.* **1991**, *94*, 1954.
(14) Wade, E. A.; Clauberg, H.; Kim, S. K.; Mellinger, A.; Moore, C. B. *J. Phys. Chem. A* **1997**, *101*, 732.
(15) García-Moreno, I.; Lovejoy, E. R.; Moore, C. B. *J. Chem. Phys.* **1994**, *100*, 8890.
(16) García-Moreno, I.; Lovejoy, E. R.; Moore, C. B. *J. Chem. Phys.* **1994**, *100*, 8902.
(17) Wade, E. A.; Mellinger, A.; Hall, M. A.; Moore, C. B. *J. Phys. Chem. A* **1997**, *101*, 6568.
(18) Wittig, C.; Nadler, I.; Reisler, H.; Noble, M.; Catanzarite, J.; Radhakrishnan, G. *J. Chem. Phys.* **1985**, *83*, 5581.
(19) Morgan, C. G.; Drabbels, M.; Wodtke, A. M. *Adv. Photochem.* **1997**, *23*, 279.
(20) Oudejans, L.; Miller, R. E.; Hase, W. L. *Faraday Discuss.* **1995**, *102*, 323.
(21) Drabbels, M.; Morgan, C. G.; McGuire, D. S.; Wodtke, A. M. *J. Chem. Phys.* **1995**, *102*, 611.
(22) Morgan, C. G.; Drabbels, M.; Wodtke, A. M. *J. Chem. Phys.* **1996**, *104*, 7460.
(23) Hu, T.; Chappel, E. L.; Sharpe, S. W. *J. Chem. Phys.* **1993**, *98*, 6162.
(24) Liu, K.; Fellers, R. S.; Viant, M. R.; McLaughlin, R. P.; Brown, M. G.; Saykally, R. J. *Rev. Sci. Instrum.* **1996**, *67*, 410.
(25) North, S. W.; Zheng, X. S.; Fei, R.; Hall, G. E. *J. Chem. Phys.* **1996**, *104*, 2129.
(26) Costen, M. L.; North, S. W.; Hall, G. E. *J. Chem. Phys.* **1999**, *111*, 6735.
(27) Chang, B.-C.; Wu, M.; Hall, G. E.; Sears, T. J. *J. Chem. Phys.* **1994**, *101*, 9236.
(28) Marr, A. J.; Sears, T. J.; Chang, B.-C. *J. Chem. Phys.* **1998**, *109*, 3431.
(29) Dixon, R. N. *J. Chem. Phys.* **1986**, *85*, 1866.
(30) Hall, G. E.; Houston, P. L. *Annu. Rev. Phys. Chem.* **1989**, *40*, 375.
(31) Brouard, M.; Duxon, S.; Enriquez, P. A.; Simons, J. P. *J. Chem. Soc., Faraday Trans.* **1993**, *89*, 1427.
(32) Gordon, R. J.; Hall, G. E. *Adv. Chem. Phys.* **1996**, *96*, 1.
(33) Hall, G. E.; North, S. W. *Annu. Rev. Phys. Chem.* **2000**, *51*, 243.
(34) Yang, S.; Bersohn, R. *J. Chem. Phys.* **1974**, *61*, 4400.
(35) Klippenstein, S. J.; Cline, J. I. *J. Chem. Phys.* **1995**, *103*, 5451.
(36) North, S. W.; Hall, G. E. *J. Chem. Phys*, **1996**, *104*, 1864.
(37) Chen, I.-C.; Green, W. H.; Moore, C. B. *J. Chem. Phys.* **1988**, *89*, 314.
(38) Chang, B.-C.; Costen, M. L.; Marr, A. J.; Ritchie, G.; Hall, G. E.; Sears, T. J. *J. Mol. Spectrosc.* **2000**, *202*, 131.
(39) Kinsey, J. L. *J. Chem. Phys*, **1977**, *66*, 2560.
(40) Supplee, J. M.; Whittaker, E. A.; Lenth, W. *Appl. Optics* **1994**, *33*, 6294.
(41) Yu, J.; Klippenstein, S. J. *J. Chem. Phys*, **1991**, *95*, 9882.
(42) Nikitin, E. E.; Troe, J. *Ber. Bunsen-Ges. Phys. Chem.* **1997**, *101*, 445.
(43) Press, W. H.; Flannery, B. P.; Teukolsky, S. A.; Vettering, W. T. *Numerical Recipies*; Cambridge University Press: Cambridge, U.K., 1986.
(44) Baer, T.; Hase, W. L. *Unimolecular Reaction Dynamics: Theory and Experiments*; Oxford University Press: Oxford, U.K., 1996; Chapter 9.
(45) Hamilton, I.; Brumer, P. *J. Chem. Phys.* **1985**, *82*, 595.
(46) Troe, J. *Ber. Bunsen-Ges. Phys. Chem.* **1996**, *101*, 438.
(47) Smith, S. C. *Faraday Discuss.* **1995**, *102*, 17.
(48) Reid, S. A.; Reisler, H. *J. Phys. Chem.* **1996**, *100*, 474.
(49) Reid, S. A.; Sanov, A.; Reisler, H. *Faraday Discuss.* **1995**, *102*, 129.
(50) Levine, R. D.; Bernstein, R. B. *Molecular Reaction Dynamics and Chemical Reactivity*; Oxford University Press: Oxford, U.K., 1987; p 274.
(51) Morgan, C. G.; Wodtke, A. M. University of California at Santa Barbara, Santa Barbara, CA. Private communication, 1996.
(52) Forsythe, K.; Klippenstein, S.; Gray, S. Argonne National Laboratory, Argonne, IL. Private communication, 2000.